# A novel shape sensing method based on principal component analysis: formulation and validation on a composite grid structure under thermal loads

*Original*
A novel shape sensing method based on principal component analysis: formulation and validation on a composite grid structure under thermal loads / Galfione, A., Esposito, M., Totaro, G., Ciminello, M., Ameduri, S., Gherlone, M.. - In: COMPUTERS & STRUCTURES. - ISSN 0045-7949. - ELETTRONICO. - 330:(2026). [10.1016/j.compstruc.2026.108324]

*Availability:*
This version is available at: 11583/3012003 since: 2026-06-13T09:53:01Z

*Publisher:*
Elsevier

*Published*
DOI:10.1016/j.compstruc.2026.108324

Computers and Structures 330 (2026) 108324

Contents lists available at ScienceDirect

Computers and Structures

journal homepage: www.elsevier.com/locate/cas

# A novel shape sensing method based on principal component analysis: formulation and validation on a composite grid structure under thermal loads

Alessio Galfione [a,*], Marco Esposito [a], Giovanni Totaro [b], Monica Ciminello [b], Salvatore Ameduri [b], Marco Gherlone [a]

[a] Department of Mechanical and Aerospace Engineering, Politecnico di Torino, Corso Duca degli Abruzzi 24, Torino, 10129, Italy
[b] Italian Aerospace Research Centre - CIRA, Via Maiorise 1, Capua (CE), 81043, Italy

## ARTICLE INFO

*Keywords:*
Shape sensing
Principal component analysis
Modal method
Thermal loads
Composite structure
Space grid structure

## ABSTRACT

This work presents the principal component analysis-based method, a novel approach for shape sensing in complex structures. Shape sensing is the process of reconstructing a structure's deformed shape from discrete strain measurements. This challenge has been addressed with various algorithms over the past three decades, each with its advantages and disadvantages. The principal component analysis-based method derives its structure from the modal method, a traditional approach, replacing the normal modes with bases obtained through a four-step process: (1) defining representative base loads (whatever their physical origin may be, whether mechanical, thermal or otherwise), (2) computing corresponding displacement fields via finite element analysis, (3) applying principal component analysis to these fields to derive an ordered set of new displacement bases, and (4) calculating the associated strain fields through further finite element simulations. The method's effectiveness is demonstrated by reconstructing the shape of a composite grid-like structure under non-uniform thermal loads with limited sensor availability. Thermal deformations are particularly relevant to the aerospace community and are largely absent from the shape-sensing literature. The principal component analysis-based method outperforms the modal method by providing an accurate solution for a complex case in which the normal modes are not valid bases for reconstructing the deformed shape.

## 1. Introduction

Engineering structures have become increasingly intelligent in recent years. The types and number of sensors installed on such structures have grown, and with them the possibilities for real-time or offline monitoring and control [6,28,36]. In parallel, the demand for real-time monitoring of structures has grown across several fields, and the aerospace sector is a clear example of this [1]. The techniques and processes with these objectives fall within the Structural Health Monitoring (SHM) field. Among them, a very useful process is called shape-sensing (or shape reconstruction), which aims to compute the deformed shape of a structure using only strains measured at discrete locations. Measuring strains is typically much easier than measuring displacements, especially during operation. Therefore, shape-sensing techniques can provide useful information for real-time monitoring and actuation of the structure, as well as deformation and load information for use in iterative design cycles [2]. A context where these methods can prove very useful is that of remotely located structures, where having an operator perform measurements or even just a visual inspection is impossible. Space structures, such as satellite components, are interesting examples because they are very remote and difficult to monitor directly. As is well known, the number of space structures has grown significantly over the last two decades, and their functional accuracy is becoming increasingly crucial across many civil and defense applications [13,33,40]. A space structure is subject to loads that are uncommon in Earth applications, especially in terms of thermal conditions. Cyclic exposure to sunlight results in widely varying temperatures, which can produce deformations very different from those generated by mechanical loads [3,9]. Real-time knowledge of these deformations can significantly improve the efficiency and effectiveness of

---

[*] Corresponding author.

*Email addresses:* alessio.galfione@polito.it (A. Galfione), marco.esposito@polito.it (M. Esposito), g.totaro@cira.it (G. Totaro), m.ciminello@cira.it (M. Ciminello), s.ameduri@cira.it (S. Ameduri), marco.gherlone@polito.it (M. Gherlone).

https://doi.org/10.1016/j.compstruc.2026.108324
Received 23 March 2026; Accepted 4 June 2026

antennas, reflectors, and solar panels, to name a few. It is therefore crucial to have SHM techniques, specifically shape-sensing, operating on such structures under thermal loads.

Over the last three decades, several shape-sensing methods have been developed. They are presented here following the four-group classification proposed by Gherlone et al. [18]. The first group includes methods that obtain displacements by directly integrating strain measurements. A remarkable effort was made here by Ko and coworkers in developing what's called Ko's Displacement Theory. The approach was initially presented for slender constant cross-section beams and then extended to include wing-boxes and plates [30]. This approach has been shown to provide accurate results with a limited number of sensors [4,25,29], but it requires the structure to be accurately approximated as a beam-like structure. The methods in the second group approximate the strain field as a linear combination of global or piecewise continuous basis functions. An a priori set of basis functions is selected, and the strain field is approximated by deriving the linear combination of such bases that best fits the measured strains. Then, the displacement field is obtained from the strain-displacement relationships, subject to appropriate Boundary Conditions (BCs). The most common choice of basis functions is probably the structure's normal modes. In this case, the shape-sensing algorithm is referred to as the Modal Method (MM), which was originally proposed simultaneously by Pisoni et al. [41] and Foss and Haugse [14]. In these works, the normal modes were experimentally determined, a process more complex, time-consuming, and expensive than computing them through a Finite Element (FE) model as commonly done in many subsequent works [5,12,15,23,34]. However, unlike the FE process, the experimental validation of the normal modes does not require knowledge of the material properties, a significant advantage. The MM is versatile since it can, in principle, be applied to any type of structure (beam-like, plate-like, or solid) and can produce accurate results with fewer strain sensors than alternatives [12]. However, it typically requires an accurate FE model of the structure and its material properties, along with a set of possible load cases to compute normal modes and select the relevant ones. The third group of shape-sensing approaches consists of methods based on Artificial Neural Networks (ANNs). The initial efforts showed a strong dependency of the accuracy on the training data [7,35]. However, exploiting the idea by Raissi et al. [43], many researchers have recently tried to include physics knowledge in the training process to reduce the required training data and to make the ANNs robust outside of the training space [22,32,42]. Research on these methods is very active, and frequent improvements are achieved by changing architectures, objective functions, and training datasets. Lastly, there is the group of methods based on a FE discrete variational principle. These methods use different kinds of variational approaches and FE approximations to perform full-field shape-sensing [39,44–47]. A quite successful method in this group is the inverse Finite Element Method (iFEM) for shear deformable plates and shell structures presented by Tessler and Spangler [45,47]. In this method, a least-squares functional, discretized by FEs and capable of accommodating arbitrarily positioned and oriented strain data, is defined. Minimizing this functional with respect to nodal Degrees Of Freedom (DOFs) enforces compatibility between the measured strains and those interpolated within each element. The iFEM was then specialized by Gherlone et al. in [19] and in [20] for the shape sensing of truss, beam, and frame structures. Moreover, it was extended to work with cylindrical and conical structures, first with an inverse shell element [26] and then with specific beam elements [11,38]. The iFEM has proven to be a very accurate and versatile method, requiring no information on material properties or loading conditions and using a discretization similar to that of the standard FE method. However, its main drawback is the greater number of strain measurements and thus sensors required to achieve accurate results compared to other methods.

These shape-sensing methods have been widely tested for the reconstruction of mechanically generated deformations, but their validation for thermal deformations is largely lacking in the literature, although some examples exist. Cerracchio et al. [9] used iFEM for the shape sensing of a composite stiffened plate under a uniform temperature variation. This work shows that the process can produce accurate results, but it might require more sensors than when reconstructing mechanical deformations. A similar conclusion is also drawn by Yu et al. [53], who reconstructed the shape of a space truss structure and two attached solar panels under mechanical and thermal loads. The authors used Ko's displacement theory for shape sensing of trusses and proposed a deformation reconstruction strategy tailored for panels with complex BCs. An experimental validation of iFEM to reconstruct thermal deformations was presented by Chen et al. [10], who proposed a technique to improve the inverse mesh definition. A large-scale antenna panel was loaded under uniform and non-uniform thermal loads, and the method showed good reconstruction accuracy. These examples show that there is interest in the technology, but there are some limiting factors for its application, specifically, reducing the number of sensors and handling complex geometries and materials.

This paper presents a novel shape-sensing method, conceptually derived as a variation of the MM, retaining many of its advantages. This new method substitutes the normal modes in the linear combination at the core of the MM with bases generated via a four-step process centered on Principal Component Analysis (PCA). Thus, the proposed method is called the PCA-based Method (PCAM). The first step is to define a set of base loads on the structure, which may be thermal, mechanical, or even different, depending on the nature of the actual loads applied. In the second step, these loads are imposed on the structure in an FE analysis to obtain the corresponding displacement fields. In the third step, PCA is performed on these displacement fields to obtain an ordered set of new deformed shapes. In the fourth step, these PCA-derived deformed shapes are then imposed on the structure in new FE analyses to obtain the corresponding strain fields. The sets of displacement and strain fields are then used for the shape-sensing procedure. Following the MM approach, the linear combination of the selected strain bases that best fits the measured strains in a least-squares sense is computed, and then a linear combination of the corresponding displacement bases is performed to reconstruct the objective displacements. Thanks to its similarity to the MM, the PCAM is expected to retain most of its properties, including its accuracy under limited sensor availability and its low computational cost, making it a very good option for real-time monitoring. In fact, the only real-time computation required for operational monitoring is a matrix-vector multiplication. Another property inherited from the MM is its versatility, since the PCAM is, in principle, applicable independently of the structure's geometry and material, as well as the load type and distribution. On the other hand, the PCAM, unlike the MM, does not require knowledge of the structure's typical loading conditions for mode selection. Moreover, the PCAM is applicable to any type of external load (mechanical, thermal, etc.), whereas MM performs poorly for non-mechanical loads.

In the literature, PCA has been widely used in direct structural analysis mainly for one objective: finding computationally efficient base shapes for linear combinations in methods such as Rayleigh-Ritz or Galerkin. These methods typically aim to solve the linear/nonlinear static or dynamic problem of determining the model degrees of freedom satisfying approximated equilibrium or motion equations, and they are the traditional alternative to the FE method [8,27,31]. This problem differs from the one investigated in the present work, i.e., shape sensing, where the degrees of freedom are reconstructed from sparse sensor strain measurements in order to best fit these to the reconstructed ones. In the context of shape sensing, Zhang et al. [54] used PCA as a preprocessing tool to expand the strain measurements, which were then used as inputs for the iFEM. This approach is fundamentally different from the method presented in this work, in which PCA is incorporated into the shape-sensing algorithm itself. More similar to the shape sensing approach presented here is that used by Galasso et al. [16], where the deformed shape is reconstructed as a linear combination of shapes generated from specific loads. However, the present contribution generalizes that approach by performing PCA on the initial distributions, resulting in less load dependency and the ability to reconstruct more complex deformations.

After presenting the formulation of the novel method, this study compares the PCAM and the MM for the shape sensing of the Carbon Fiber Reinforced Plastic (CFRP) grid structure of a satellite boom segment under a non-uniform thermal load. This structure, called the LRBOOM, is designed to support a large deployable satellite reflector and, as a result, is subject to thermal deformations from solar radiation. Its complex geometry, the anisotropic material, the limited number of sensors, the type of load, and, above all, the combination of these aspects pose interesting challenges for this field. It is in these conditions that the MM typically excels over alternatives, but under this case, as shown in the rest of the study, the results are inaccurate, if not completely wrong, underscoring the need for a new approach. This new approach is provided by the PCAM, which can reconstruct the structure's deformed shape under these complex conditions. Moreover, this study shows that the computational cost of the preliminary steps required to obtain the PCA-derived bases is comparable to that of the normal modes they replace.

Therefore, there are two main novel aspects to this work. First, the proposed shape-sensing method, PCAM, is a new approach that adds additional information about the structure's behavior to the reconstruction process. The method, generally applicable to any type of structure and load case, uses PCA, a well-known data-processing technique that has not been used in a shape-sensing algorithm. Second, the validation of this method is proposed for a space structure under non-uniform thermal loading, a test case particularly relevant to the structural health monitoring and aerospace communities but crucially missing in the literature.

In line with the objectives presented above, this paper begins with a description of the MM in Section 2. Then, Section 3 describes the PCAM, highlighting the differences with the MM. Following this, the numerical test case is presented in Section 4, highlighting the problems of the MM in this scenario. Finally, the results are discussed, and future improvements to the method are proposed in Sections 5 and 6, respectively.

## 2. Modal method

The Modal Method (MM) has been thoroughly described in many papers, from the ones in which it was first presented [14,41], to more recent ones [12,18]. Therefore, the aim of this section will not be to describe the method in a thorough manner but to provide a schematic (Fig. 1) that facilitates the explanation of the alternative proposed here. Some details are omitted and can be found in the work by Esposito and Gherlone [12], which is also used as the main reference for the description proposed.

As mentioned in the introduction, the MM reconstructs the deformed shape as a linear combination of the structure's normal modes. The core of the method derives the coefficients of the linear combination by finding, in a least-squares sense, the optimal set of coefficients that best fit the measured strain values. The first step is to obtain the structure's normal modes. Although it is possible to experimentally derive the normal modes [14,41], it is easier and more common to compute them through a FE analysis. If the FE approach is used, a model must be built and a modal analysis performed. To numerically compute the normal modes, BCs, and elastic material properties should be defined in the FE model. From this analysis, a set of normal modes of the structure and the corresponding strain fields are obtained. Information about displacements and strain for each mode is saved in two matrices, where each column corresponds to a mode. First is the displacement modal shapes matrix (simply known as the modal matrix), $\mathbf{\Phi}_d$, of size $D \times M$, where $D$ is the number of displacements exported from the FE simulation for each mode and $M$ is the number of modes computed. Then, there is the strain modal shape matrix, $\mathbf{\Phi}_s$, of size $S \times M$, where $S$ is the number of strain values exported from the FE simulation for each mode. Then, it is possible to write the displacement ($\boldsymbol{w}$) and strain ($\boldsymbol{\varepsilon}$) vectors of the reference deformed shape in terms of a linear combination of the modal matrices, as in Eqs. (1) and (2), respectively. In these equations, $\boldsymbol{q}$ is the vector of coefficients of the linear combination, also called modal coordinates.

$$\boldsymbol{w} = \mathbf{\Phi}_d \boldsymbol{q} \tag{1}$$

$$\boldsymbol{\varepsilon} = \mathbf{\Phi}_s \boldsymbol{q} \tag{2}$$

From Eq. (2), the modal coordinates can be computed as in Eq. (3).

$$\boldsymbol{q} = \mathbf{\Phi}_s^{-1} \boldsymbol{\varepsilon} \tag{3}$$

However, typically $\mathbf{\Phi}_s$ is a non-square matrix and is therefore not invertible. The typical case involves having more strain sensors than modes ($S > M$), which can be solved in the least-squares sense using the Moore-Penrose pseudoinverse in place of standard inversion, resulting in Eq. (4).

$$\boldsymbol{q} = \left(\mathbf{\Phi}_s^T \mathbf{\Phi}_s\right)^{-1} \mathbf{\Phi}_s^T \boldsymbol{\varepsilon} \tag{4}$$

Then, substituting Eq. (4) into Eq. (1), (5) is obtained to compute the reconstructed displacements.

$$\boldsymbol{w} = \mathbf{\Phi}_d \left(\mathbf{\Phi}_s^T \mathbf{\Phi}_s\right)^{-1} \mathbf{\Phi}_s^T \boldsymbol{\varepsilon} \tag{5}$$

The next step involves selecting the modes to include in the linear combination. The most common mode selection procedure, presented by Bogert et al. [5], selects modes based on their strain energy contributions to a reference static deformation. To do so, the reference solution must be selected as representative of the load cases to be reconstructed. Although this method appears to require knowledge of the deformed shape (the solution to the problem) as input, that is not entirely true. In fact, typically, to design a structural component, knowledge of the most common or most critical load cases is required, and those load cases can be used as a reference for the mode selection procedure. It is also possible to consider multiple load cases in the mode selection as presented by Galfione et al. [17]. As mentioned above, the modes are selected based on the contribution to the strain energy of a reference deformed shape. This process is done by ordering the deformed shapes in terms of strain energy contribution, defining a strain energy threshold $e_{th}$, then selecting the first $M_{sel}$ modes as defined in Eq. (6). In this equation, $e_i$ is the fraction of strain energy contribution of the ith mode.

$$\sum_{i=1}^{M_{sel}-1} e_i < e_{th} \qquad \text{and} \qquad \sum_{i=1}^{M_{sel}} e_i \geq e_{th} \tag{6}$$

A remark must be made regarding the computation of the strain energy from a structural FE analysis in which thermal loads are applied. The strain energy output from the software used in this study, MSC Nastran, is not the quantity required for the mode selection criterion, and a few additional steps are needed to obtain the correct value. The details, which might differ in other software, are discussed in Appendix A. After the mode selection, the two modal matrices, $\mathbf{\Phi}_d$ and $\mathbf{\Phi}_s$, will have $M_{sel}$ columns, where $M_{sel}$ is the number of selected modes. The last missing piece is the vector of measured strains. These values, either measured experimentally on a structure or exported from a reference FE analysis, are put together in a column vector $\boldsymbol{\varepsilon}$. Using these quantities, the reconstructed displacements can be computed using Eq. (5), where the modal matrices contain only the selected modes.

It is important to note that once the sensor locations and the modes are selected, the modal matrices $\mathbf{\Phi}_d$ and $\mathbf{\Phi}_s$, used in (5), are fixed, and the computation is reduced to a matrix-vector multiplication. As mentioned above, this makes the MM highly efficient and well-suited for real-time monitoring.

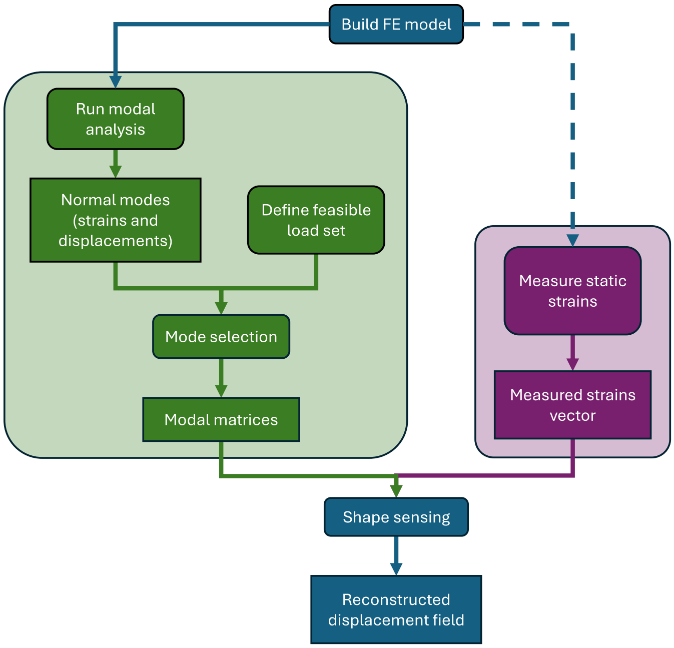

**Fig. 1.** Diagram of the MM procedure.

## 3. Principal component analysis method

In this section, the Principal Component Analysis-based Method (PCAM), an alternative shape-sensing approach, is presented. In this method, unlike MM, the bases are the deformed shapes obtained from a PCA rather than the normal modes. The green part of the diagram in Fig. 1 is then modified to yield the diagram shown in Fig. 2, which illustrates the PCAM procedure. The process starts from the definition of a generic set of $N_l$ load cases. Once the load cases are defined, they are applied to a FE model of the structure. A static structural FE analysis is performed for each load case to obtain $N_l$ deformed shapes. The displacement fields of each deformed shape are assembled in the matrix $\boldsymbol{\Psi}_d$ of size $D \times N_l$, where $D$ is the number of displacement terms for each deformed shape. Then, the PCA is performed on the $\boldsymbol{\Psi}_d$ matrix. This process is defined as an orthogonal linear transformation that maps the data to a new coordinate system such that the greatest variance, under some scalar projection of the data, lies on the first coordinate (the first principal component), the second greatest variance on the second coordinate, and so on. This procedure is commonly used to reduce the dimensionality of a dataset, retaining most of its variation [24], which is also its purpose in this work. The PCA requires the data, in this case the deformed shapes, to be centered around the origin. This preliminary step is done by computing the mean of each row of $\boldsymbol{\Psi}_d$ and subtracting the vector of means from each column. Then, the principal components and the corresponding coefficients are computed using the MATLAB built-in *svd* function, with the *econ* option active, which performs the compact Singular Value Decomposition (SVD) [52]. This approach is equivalent to using the MATLAB built-in *pca* function. The resulting decomposition of the $\boldsymbol{\Psi}_d$ matrix is

$$\boldsymbol{\Psi}_d = \boldsymbol{U}\boldsymbol{\Sigma}\boldsymbol{V}^T \tag{7}$$

Here, $\boldsymbol{\Sigma}$ is an $r \times r$ diagonal matrix, where $r$ is the rank of $\boldsymbol{\Psi}_d$. In $\boldsymbol{\Sigma}$, the diagonal elements are the non-zero singular values of $\boldsymbol{\Psi}_d$ and are ordered in decreasing order. Then, $\boldsymbol{U}$ is a $D \times r$ semi-orthogonal matrix, which means that the vectors in the smaller dimension are orthonormal vectors, in this case, the columns. The columns of $\boldsymbol{U}$ are the left singular vectors of $\boldsymbol{\Psi}_d$ for the corresponding singular values stored and ordered in $\boldsymbol{\Sigma}$. Similarly, $\boldsymbol{V}$ is an $N_l \times r$ semi-orthogonal matrix, which, also in this case, means that the columns are orthonormal vectors. The columns of $\boldsymbol{V}$ are the right singular vectors of $\boldsymbol{\Psi}_d$ for the corresponding singular values. In this context, the left singular vectors are the relevant ones, since, going back to the structural interpretation, they define new deformations ordered by the variance of the initial data on them. Therefore, the columns of $\boldsymbol{U}$ are the new bases used in place of the normal modes in the shape reconstruction process. To select which bases to include in the reconstruction, a threshold ($\sigma_{th}$) on the cumulative variance can be imposed, selecting the first $B_{sel}$ bases using Eq. (8), where $\Sigma_{ii}$ is the $i$-th diagonal element of $\boldsymbol{\Sigma}$.

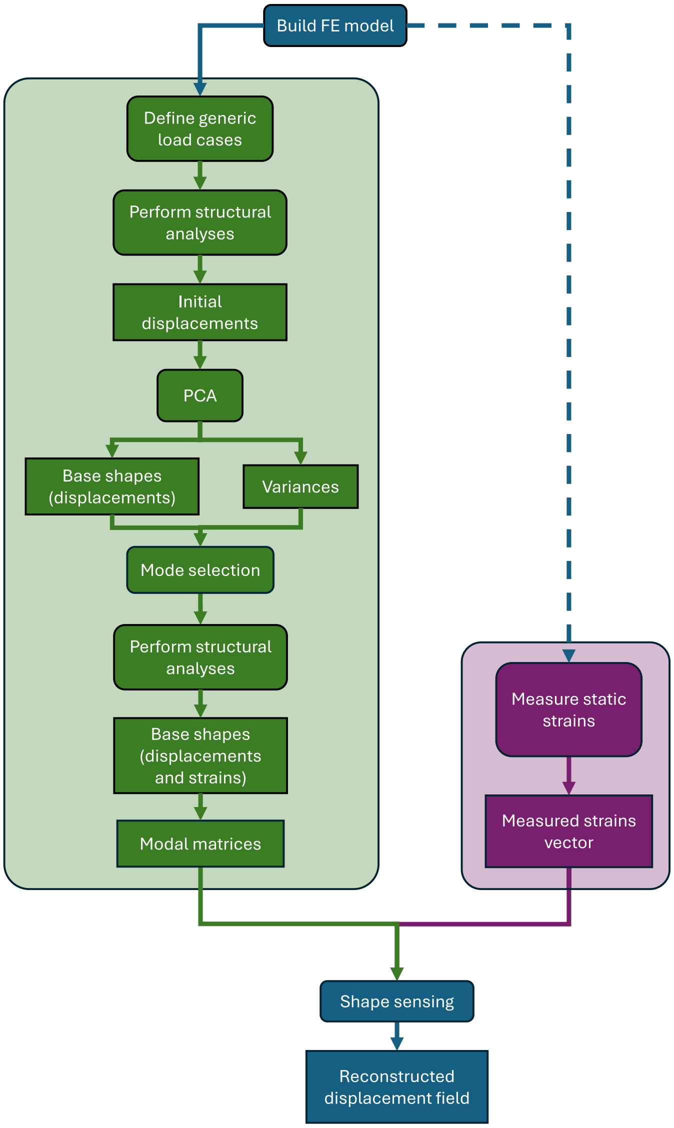

**Fig. 2.** Diagram of the PCAM procedure.

$$\sum_{i=1}^{B_{sel}-1} \Sigma_{ii} < \sigma_{th} \qquad \text{and} \qquad \sum_{i=1}^{B_{sel}} \Sigma_{ii} \geq \sigma_{th} \tag{8}$$

The remaining quantities needed to define the “modal” matrices are the strain fields corresponding to the selected bases, which are used to build matrix $\boldsymbol{\Psi}_s$. To obtain them, the displacement fields computed with the PCA (the first $B_{sel}$ columns of $\boldsymbol{U}$) are imposed on the FE model, and the strains at the relevant locations are computed through a static structural analysis.

Since PCAM requires more analysis steps than MM, it is of interest to compare their computational costs. The MM requires solving an eigenvalue problem, which is typically much more expensive than a

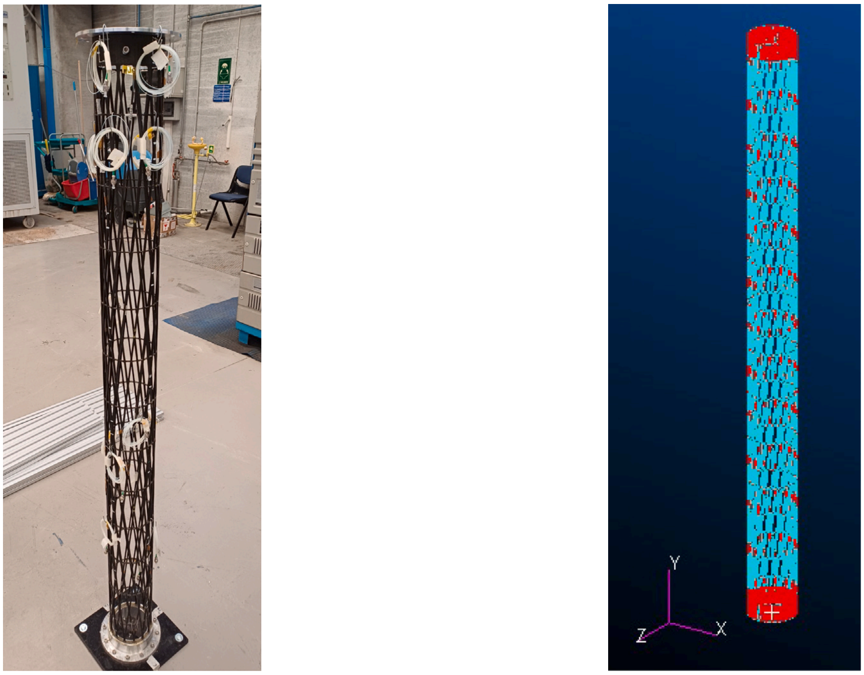

(a) Picture of the LRBOOM with fiber-optic strain sensors installed. The top metallic flange present in this picture is not modeled because it is not part of the composite structure investigated in the study.

(b) FE model of the LRBOOM in MSC PATRAN

**Fig. 3.** The LRBOOM.

static structural analysis. On the other hand, the PCAM requires solving two sets of $N_l$ static structural analyses. The first set consists of static structural analyses in which initial loads are applied to the structure. Conversely, the second set consists of static structural analyses in which displacements are imposed at all nodes, except at least one DOF, which should be left free to have a non-empty system to solve. Moreover, the number of analyses to solve in this second set can be reduced to $B_{sel}$ if the strain fields are computed only for the selected bases. The computational costs in these problems lie in different steps, whose duration depends on the number of natural modes computed or the number of load cases considered. To provide a benchmark, the computational times for the analyses performed here are presented in Section 5.

The remaining steps of the process are identical to those for the MM, but use the selected PCA-generated bases instead of the normal modes. The measured strain vector $\boldsymbol{\varepsilon}$ is built, and the pseudo-inversion and matrix multiplication are performed to obtain the reconstructed displacement field $\boldsymbol{w}$ using Eq. (5), which becomes Eq. (9) using the PCAM notation. In this equation, $\boldsymbol{\Psi}_d$ has size $D \times B_{sel}$, while $\boldsymbol{\Psi}_s$ has size $S \times B_{sel}$.

$$\boldsymbol{w} = \boldsymbol{\Psi}_d (\boldsymbol{\Psi}_s^T \boldsymbol{\Psi}_s)^{-1} \boldsymbol{\Psi}_s^T \boldsymbol{\varepsilon} \tag{9}$$

As for the MM, the matrices $\boldsymbol{\Psi}_d$ and $\boldsymbol{\Psi}_s$ depend only on the bases and sensor locations; therefore, once these are selected, the computation reduces to a matrix-vector multiplication. This makes the PCAM equally valid for real-time monitoring as the MM.

## 4. Test case

This section presents the components used to validate the proposed approach by describing the FE model in detail. Then, the process for simulating a lab test of the component under non-uniform thermal loads is described. The rationale behind the test setup is to reproduce, in a laboratory-friendly way, the loading condition to which the component would be subjected when laterally exposed to sunlight. Clearly, the temperatures involved would not be equivalent to the operational ones, but the structural behavior should provide an idea of what to expect in the actual case. Moreover, the scope of this paper is to provide a practically relevant test case for the proposed methodology, not to test the structure under real operational loads. Finally, the processes to obtain the basis functions for the MM and the PCAM are specialized to this case, and the Optimal Sensor Placement (OSP) procedure is presented.

### *4.1. Test component*

The test case for the proposed methodology is a CFRP grid satellite boom segment for large deployable reflectors, called LRBOOM (Fig. 3(a)). The component, examined here numerically, is manufactured using a specific winding technology that endows it with peculiar thermal properties [16,21]. The manufacturing process aligns the fibers along the length direction of each element, resulting in a unidirectional composite everywhere except at the crossing points. There, the fibers are oriented in two “in-plane” directions, resulting in different material properties. Since the Coefficient of Thermal Expansion (CTE) of the material is negative in the fiber direction and positive in the transverse directions, at crossing locations, there is a change in the tangential CTE. This aspect is the most probable cause, combined with the geometry, for the complex thermal behavior of the structure. To perform the analyses required in this study, an FE model (Fig. 3(b)) of the component is used. The structure is modeled with three-dimensional elements to capture the through-thickness behavior and the material orthotropy.

A zoom on the end section of the model, shown in Fig. 4, allows one to see all the element types used in the discretization of the LRBOOM. The light blue elements are hexahedral, and the red ones are wedges. Among the hexahedral elements, two kinds are distinguished for their purpose in the structure and their orientation. First, the helicoidal struts wind around the structure between the two ends; their elements are here called helic elements. Second, the hoop elements are part of stiffening hoops added to the structure orthogonally to the main beam direction. These two element types have different dimensions, but the same local

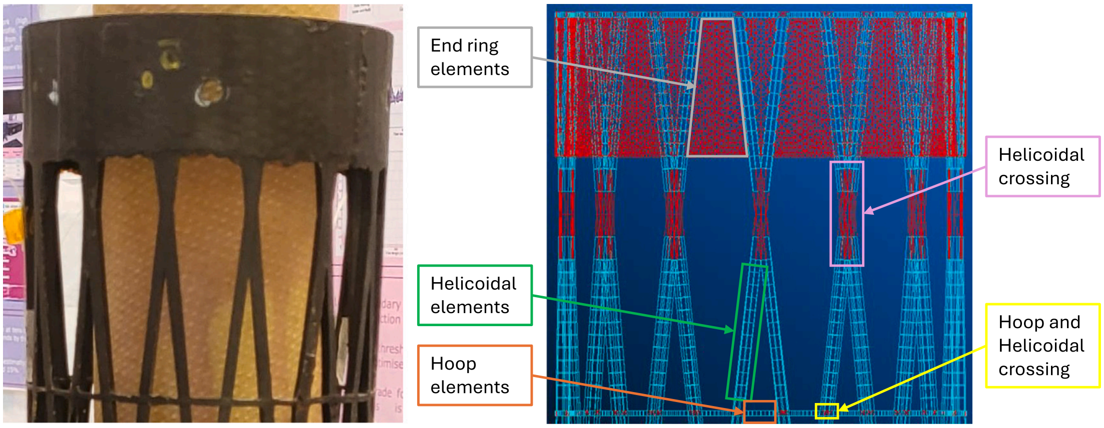

**Fig. 4.** Zoom on the LRBOOM end. On the left, a picture of the actual component, on the right, part of the model showing the different kinds of FEs, from MSC PATRAN.

**Table 1**
Material properties of the orthotropic hexahedral elements.

| Property | Value | Description |
|---|---|---|
| $E_1$ | 180 GPa | Longitudinal elastic modulus |
| $E_2$ | 6.1 GPa | Transverse elastic modulus |
| $E_3$ | 6.1 GPa | Out-of-plane elastic modulus |
| $G_{12}$ | 3.8 GPa | In-plane shear modulus |
| $G_{23}$ | 2.5 GPa | Out-of-plane shear modulus |
| $G_{31}$ | 3.8 GPa | Transverse shear modulus |
| $\nu_{12}$ | 0.25 | In-plane Poisson's ratio |
| $\nu_{13}$ | 0.25 | Out-of-plane Poisson's ratio |
| $\nu_{23}$ | 0.60 | Transverse Poisson's ratio |
| $\rho$ | $1450\,kgm^{-3}$ | Density |
| $CTE_{11}$ | $-2E–7K^{-1}$ | Longitudinal CTE |
| $CTE_{22}$ | $5.4E–5K^{-1}$ | Transverse CTE |
| $CTE_{33}$ | $5.4E–5K^{-1}$ | Out-of-plane CTE |
| $\kappa_{11}$ | $30\,Wm^{-1}K^{-1}$ | Longitudinal thermal conductivity |
| $\kappa_{22}$ | $0.31\,Wm^{-1}K^{-1}$ | Transverse thermal conductivity |
| $\kappa_{33}$ | $0.31\,Wm^{-1}K^{-1}$ | Out-of-plane thermal conductivity |

**Table 2**
Material properties of wedge elements.

| Element type | Property | Value | Description |
|---|---|---|---|
| Helic-Helic and Helic-Hoop Crossings (Isotropic) | $E$ | 170 GPa | Elastic modulus |
| | $\nu$ | 0.30 | Poisson's ratio |
| | $G$ | 65 GPa | Shear modulus |
| | $\rho$ | $1700kgm^{-3}$ | Density |
| | $CTE$ | $-2E--7K^{-1}$ | CTE |
| | $\kappa$ | $30Wm^{-1}K^{-1}$ | Thermal conductivity |
| End Rings (Orthotropic) | $E_1$ | 15 GPa | Out-of-plane elastic modulus |
| | $E_2$ | 30 GPa | Longitudinal elastic modulus |
| | $E_3$ | 30 GPa | Transverse elastic modulus |
| | $G_{12}$ | 2 GPa | Out-of-plane shear modulus |
| | $G_{23}$ | 3.2 GPa | In-plane shear modulus |
| | $G_{31}$ | 2 GPa | Out-of-plane shear modulus |
| | $\nu_{12}$ | 0.25 | In-plane Poisson's ratio |
| | $\nu_{13}$ | 0.25 | Out-of-plane Poisson's ratio |
| | $\nu_{23}$ | 0.60 | Transverse Poisson's ratio |
| | $\rho$ | $1650\,kgm^{-3}$ | Density |
| | $CTE_{11}$ | $5.0E–5K^{-1}$ | Out-of-plane CTE |
| | $CTE_{22}$ | $4.5E–6K^{-1}$ | Longitudinal CTE |
| | $CTE_{33}$ | $4.5E–6K^{-1}$ | Transverse CTE |
| | $\kappa_{11}$ | $0.31\,Wm^{-1}K^{-1}$ | Out-of-plane thermal conductivity |
| | $\kappa_{22}$ | $30\,Wm^{-1}K^{-1}$ | Longitudinal thermal conductivity |
| | $\kappa_{33}$ | $30\,Wm^{-1}K^{-1}$ | Transverse thermal conductivity |

material properties, shown in Table 1. In both cases, the material 1 direction is parallel to the fibers, while the material 3 direction is radial, pointing outward, and the missing direction is derived by the right-hand rule. On the other hand, the wedge elements are used to model three parts of the structure: the crossings of two helicoidal struts (helic-helic crossing elements), the crossing of a helicoidal strut and a stiffening hoop (helic-hoop crossing elements), and the end rings (end ring elements). The end rings are made of bands of plain-weave fabric and connect the LRBOOM to other similar segments of the boom assembly via specific interfaces. For the current demonstrator, metallic flanges are bolted to the end rings and used for constraints or load applications. The overall CFRP grid structure, thus including the end rings, is manufactured by dry robotic winding and resin infusion (the dry robotic winding process is covered by a patent filed by CIRA). Therefore, the properties of the end rings are not dominated by a single dimension (as in helic and hoop elements), but rather by two dimensions. The material properties for the wedge elements are presented in Table 2, divided by type of element. A cylindrical coordinate system aligned with the boom is used to define the material coordinate system of the end ring elements, the only anisotropic wedge elements. This means that material coordinate 1 is radial, material coordinate 2 is tangential, and material coordinate 3 is aligned with the main direction of the boom.

### *4.2. Thermal test*

As mentioned above, this test aims to simulate a laboratory test in which the LRBOOM structure is laterally irradiated by two halogen lamps. The simulation is performed in two steps. First, a steady-state thermal analysis is performed to obtain a temperature distribution on the LRBOOM structure. Then, a static structural analysis is performed imposing the temperature distribution obtained in the previous step as nodal loads. From the results of this second analysis, the strain measurements for shape sensing are extracted, mimicking the experimental strains. Moreover, the displacements are used as a reference for numerically validating the method.

#### *4.2.1. Thermal analysis*

The steady-state thermal analysis is carried out in the commercial FE software ANSYS Mechanical. The FE model is presented in Fig. 6(a), where the two cylinders on the left represent the halogen lamps and the components at the bottom of the LRBOOM are the clamping supports. The lamps are discretized using shell elements: triangular elements on the radiating surface (dark green in the figure) and rectangular elements on the reflective tube (gray in the figure). The thermal conductivity of the reflective tube is defined as isotropic and equal to $60.5Wm^{-1}K^{-1}$. The base supports are discretized using hexahedral elements in the rectangular plate (orange in the figure) and tetrahedral elements in the internal and external flanges (gray and yellow, respectively). The

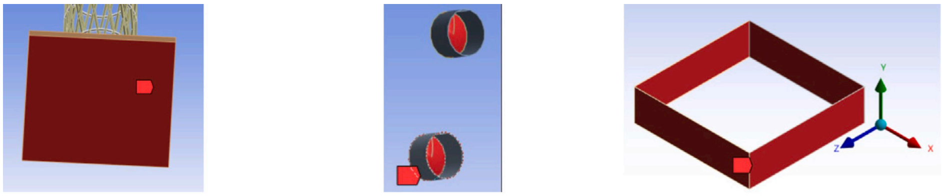

(a) In red, the surfaces to which BC 1.a is applied (b) In red, the surfaces to which BC 1.b is applied (c) In red, the surfaces to which BC 1.c is applied

(d) In blue, the surfaces to which BC 2.a is applied (e) In blue, the surfaces to which BC 2.b is applied

(f) In blue, the surfaces to which BC 2.c is applied (g) In blue, the surfaces to which BC 2.d is applied

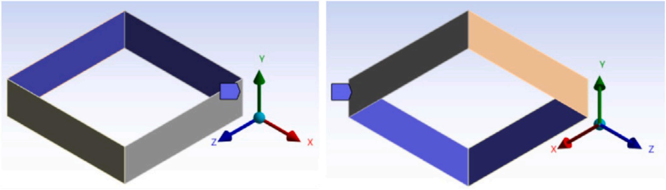

(h) In blue, the surfaces to which BC 2.e is applied

**Fig. 5.** Application regions of the thermal BCs.

LRBOOM model is identical to that presented in Section 4.1, as it is imported into ANSYS by reading the.bdf file (the MSC NASTRAN input file). The thermal conductivity of all the base components is also set to $60.5 W\,m^{-1}K^{-1}$. Finally, to model radiation to the ambient, walls are defined around the component at a large distance (more than $10\ m$) and discretized using quadrilateral shell elements. Two types of BCs are used in this model. They are listed here, and the application regions are shown in Fig. 5.

1. Fixed temperatures
   (1) Bottom surface of the base plate at room temperature ($T_r = 22\,°C$)
   (2) Lamp radiating surface at lamp temperature ($T_l = 500\,°C$)
   (3) Walls at room temperature ($T_r = 22\,°C$)
2. Radiation
   (1) Lamp radiating surface ($\epsilon_{rad} = 0.9$)
   (2) Lamp reflecting tube ($\epsilon_{rad} = 0.9$)
   (3) LRBOOM inner faces facing the lamps ($\epsilon_{rad} = 0.89$)
   (4) LRBOOM outer faces facing the lamps ($\epsilon_{rad} = 0.89$)
   (5) Walls ($\epsilon_{rad} = 0.6$)

In the definition of the BCs, $\epsilon_{rad}$ is the emissivity of the surface. The initial temperature is defined as equal to room temperature $T_i = T_r = 22°C$, and all the radiation BCs are defined as surface to surface in the same enclosure.

The output of this steady-state thermal analysis is a nodal temperature field at all nodes of the LRBOOM structure, shown in Fig. 7(a). This temperature field is used as an external load in the static structural analysis.

#### 4.2.2. *Structural analysis*

The static structural analysis is performed using the FE commercial software MSC Patran/Nastran. The temperature distribution obtained from the steady-state thermal analysis is exported from ANSYS Mechanical and applied as a nodal load in the static structural analysis. In this analysis, the model of the LRBOOM is the one presented in Section 4.1, the nodes of the bottom end rings (in the green square in Fig. 6(b)) are constrained by setting all DOFs to 0, and the initial temperature is set at $T_i = 22\,°C$. As a result of the temperature variation, a deformed shape is obtained. The result of this FE analysis provides both the input strains for the shape reconstruction process and the reference displacements for numerical validation, since this is the shape to reconstruct. Displacements are exported at all nodes of the structure, whereas strains are exported only at locations that would best permit strain-sensor installation. The nodes at which strains are exported are those that have two characteristics: they are only nodes of helic elements (defined in Section 4.1), and they are at the middle of the outside faces of the helicoidal struts. In Fig. 8, the nodes at which strains are exported are highlighted in orange. Since the struts are very slender, and therefore, the longitudinal strain is expected to be the most relevant component, the longitudinal strains at these nodes are obtained by exporting the longitudinal component (*X-component* in *Element IJK*, the standard local element reference frame in Patran) with the default MSC Patran 2024.2 settings, meaning the *Average Definition* is performed on *All Entities*, using the *Derive/Average* method and the

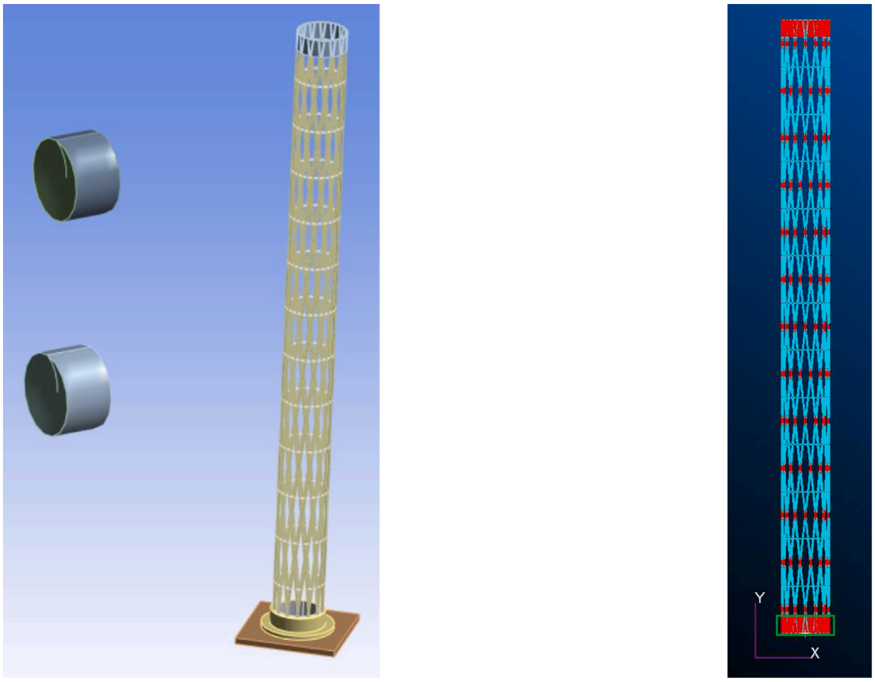

(a) Model of the LRBOOM used for the steady state thermal analysis, with the two lamps and the base in ANSYS

(b) Model of the LRBOOM used for the static structural analysis in MSC Nastran. The green square indicates the constrained nodes.

**Fig. 6.** LRBOOM models used in the FE analyses.

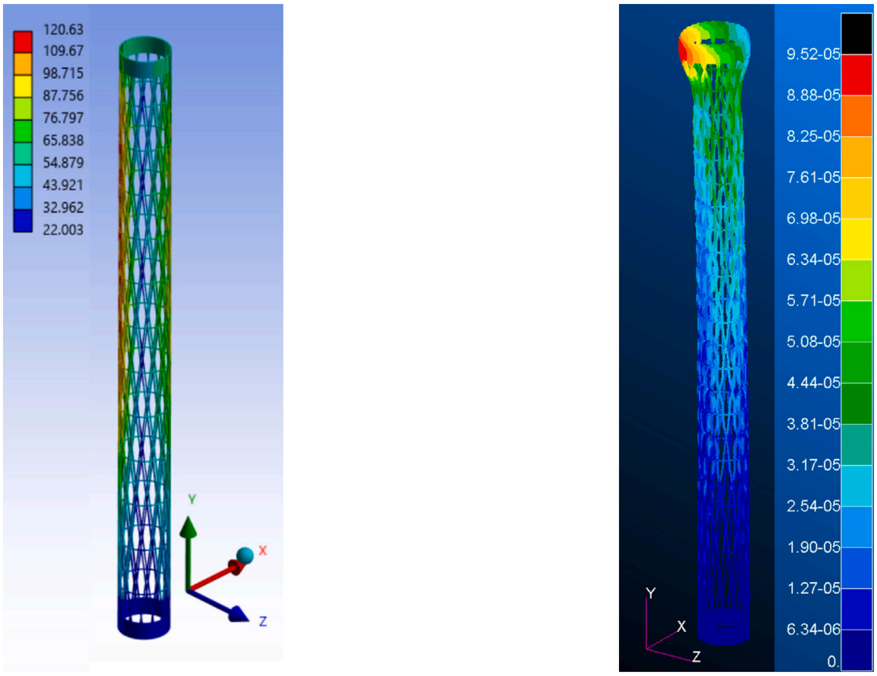

(a) Temperature distribution resulting from the steady-state thermal analysis. The colormap is in [$^\circ C$].

(b) Deformed shape resulting from imposing the temperatures as thermal loads. It is the reference deformed shape to reconstruct. The colormap indicates displacement magnitudes in [$m$].

**Fig. 7.** Results of the FE analyses on the LRBOOM.

*Shape Function* extrapolation. The words or groups of words in italics in the previous sentence represent software settings. The deformed shape resulting from this analysis, which is also the reference deformed shape to reconstruct, is shown in Fig. 7(b). This shape is characterized by three macroscopically visible phenomena: (a) Axial shrinking due to overall temperature increase, (b) global bending due to the temperature

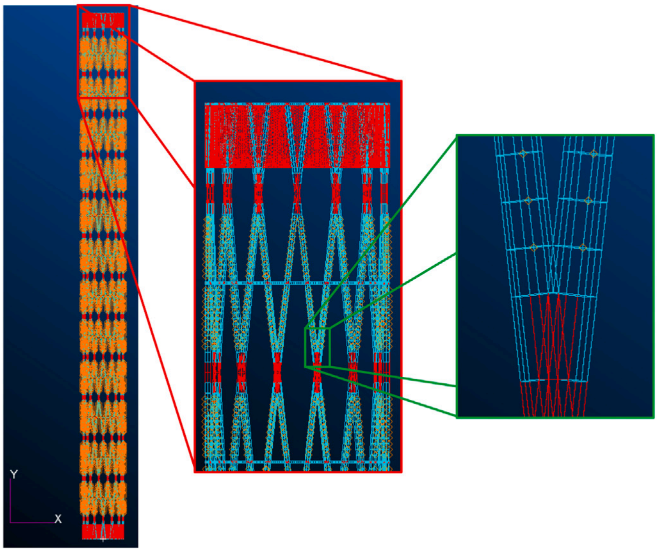

(a) Side view with close-ups

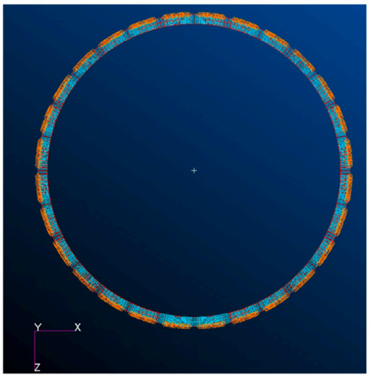

(b) Top view

**Fig. 8.** In Orange are the nodes at which strain values are exported, from two different views.

gradient between the radiated and shaded sides, and (c) cross-section dilation at the free end ring due to the in-plane CTEs being positive and one order of magnitude larger than the axial CTE of the helic elements. Additionally, local phenomena at the intersection of different kinds of elements are also present and will be relevant in the shape sensing process.

### 4.3. Normal modes basis

To implement the MM, the strain and displacement fields of a set of normal modes of the structure are required. In this case, this information is obtained through a modal analysis of the structure in the commercial FE software MSC Patran/Nastran, using the model described in Section 4.2.2. The first 100 modes of the structure are computed, and displacement and strain fields for each mode are exported to MATLAB for the shape sensing process. Displacements and strains are exported with the same approach presented in Section 4.2.2. This means that displacements are exported at all nodes, while strains are exported only at certain nodes shown in Fig. 8. The modes are then selected based on their strain-energy contributions, following the procedure described in Section 2. Different thresholds on the strain energy contributions result in a different number of selected modes, and the results of this selection process are shown in Section 5, while the relevant modes and their strain energy contributions are presented in Appendix B.

### 4.4. PCA-derived bases

To generate the PCA-derived bases, the process described in Section 3 is followed. The first step is the definition of the load cases, in this case, temperature distributions, to generate the starting set of deformations. Here, the temperature distributions are defined by exploiting the structure's two primary directions. A first set of temperature distributions is defined as varying along the axial direction ($Y$) of the LRBOOM (Fig. 3(b)), with $Y = 0$ at the base of the lower end of the structure (on the clamp side). These temperature distributions are defined using Lagrange polynomial bases as follows. Consider $N$ interpolation nodes at coordinates $Y_1, Y_2, \dots, Y_N$. Then, define the normalized coordinate $\eta$ in $[-1, 1]$ using Eq. (10).

$$\eta = 2\frac{Y - Y_1}{Y_N - Y_1} - 1 \tag{10}$$

Then, the normalized coordinate of the $k$-th interpolation node, $\eta_k$, is computed using Eq. (11).

$$\eta_k = 2\frac{Y_k - Y_1}{Y_N - Y_1} - 1 \tag{11}$$

Given $N$ interpolation nodes, $N$ Lagrange polynomial bases exist, each associated with a node. The Lagrange polynomial basis associated with node $k$ when $N$ interpolation nodes are used is defined by Eq. (12).

$$L_k^N(\eta) = \prod_{j=1, j\neq k}^{N} \frac{\eta - \eta_j}{\eta_k - \eta_j} \tag{12}$$

Here, Lagrange polynomials for $N = 2, 3, 4$ equidistant interpolation nodes are used, meaning a total of nine temperature distributions are generated this way. The two external nodes are always located at $Y_1 = 0$ and $Y_N = L$, where $L$ is the length of the LRBOOM. A final step is performed on the temperature distributions generated with this approach; they are normalized between 0 and 1.

The second set of temperature distributions is defined to vary along the tangential (angular) direction $\vartheta$, following a similar approach. In this case, trigonometric basis functions are defined as follows. Consider $N$ equidistant interpolation nodes $\Theta_1, \Theta_2, \dots, \Theta_N$ on the angular coordinate $\Theta$ of the LRBOOM, which spans $[-\pi, \pi]$. Then, define the translated coordinate $\vartheta$ in $[0, 2\pi]$ using Eq. (13).

$$\vartheta = \Theta + \pi \tag{13}$$

Then, the translated coordinate of the $k$-th interpolation node, $\vartheta_k$, is computed using Eq. (14).

$$\vartheta_k = \Theta_k + \pi \tag{14}$$

Given $N$ interpolation nodes, $N$ trigonometric basis functions are defined. Eq. (15) defines the basis function associated with the $k$-th interpolation node, when N interpolation nodes are used.

$$T_k^N(\vartheta) = \begin{cases} \frac{1}{N}\left(1 + 2\sum_{m=1}^{\frac{N-1}{2}} \cos\left(m(\vartheta - \vartheta_k)\right)\right), & \text{if N is odd} \\ \frac{1}{N}\left(1 + 2\sum_{m=1}^{\frac{N}{2}-1} \cos\left(m(\vartheta - \vartheta_k)\right) + \cos\left(\frac{N}{2}(\vartheta - \vartheta_k)\right)\right), & \text{if N is even} \end{cases} \tag{15}$$

Similarly to before, the trigonometric basis functions are computed for $N = 2, 3, 4$ equidistant nodes whose translated coordinates $\vartheta_k$ are defined as

$$\vartheta_k = \frac{2\pi(k-1)}{N} \tag{16}$$

This results in nine temperature distributions of this second kind again. Then, the temperature distributions obtained from the basis functions are normalized to the [0,1] range. Lastly, two uniform temperature

**Table 3**
Error metrics and modes selected for varying basis selection thresholds for the MM and PCAM when all sensor locations are used.

| Method | Basis selection threshold | # Bases selected | NRMSE | MDE |
|---|---|---|---|---|
| MM | 0.0002% | 1 | 17.57% | 77.90% |
| MM | 0.0003% | 3 | 19.57% | 69.32% |
| MM | 0.0004% | 5 | 20.31% | 64.08% |
| MM | 0.0005% | 11 | 21.17% | 51.39% |
| MM | 0.0006% | 100 | 26.83% | 41.00% |
| PCAM | 70% | 2 | 9.04% | 55.92% |
| PCAM | 80% | 2 | 9.04% | 55.92% |
| PCAM | 90% | 3 | 6.67% | 51.59% |
| PCAM | 95% | 5 | 4.03% | 14.81% |
| PCAM | 99% | 6 | 3.96% | 8.35% |
| PCAM | 99.9% | 7 | 3.96% | 6.80% |

distributions are added: the first with a uniform value of 0, and the second with a uniform value of 1. Therefore, the resulting set contains 20 temperature distributions between 0 and 1.

In the second step, these temperature distributions are applied as loads in the commercial FE software MSC Patran/Nastran to the model presented in Section 4.2.2, with an initial temperature $T_i = 0$. The resulting deformed shapes are exported by stacking the three displacements at each node in a column vector and assembling them in $\Psi_d$, a matrix of size $D \times N_l$, where $D$ is the number of displacement terms per deformed shape and $N_l = 20$ is the number of temperature distributions and thus of deformed shapes generated.

Subsequently, the SVD of the $\Psi_d$ matrix is computed as shown in Eq. (7). As a result, the $U$ matrix is obtained, whose $N_l$ columns can be used as bases for the shape sensing process. Then, imposing a threshold $\sigma_{th}$ on the cumulative variance, only the first $B_{sel}$ bases are selected for the shape sensing process, as defined in Eq. (8). As for the MM, the basis selection results are presented in Section 5 for a range of thresholds. Moreover, the relevant bases and their variances are presented in Appendix B.

The final quantities required for the shape-sensing process are the strain fields corresponding to each selected basis. The displacement fields obtained from the PCA process are imposed on the nodes of the model in MSC Nastran, and a static analysis is performed to compute the strain field.

Finally, the PCA-generated bases and the corresponding strain fields are used to build the $\Psi_d$ and $\Psi_s$ matrices and perform the shape sensing process by matrix pseudo-inversion, using Eq. (9).

### 4.5. Optimal sensor placement

An OSP is studied to achieve accurate results with a limited number of sensors, using both the MM and the PCAM. For each method, the OSP was performed using the multiobjective genetic algorithm implemented in the *gamultiobj* MATLAB function [48], following the approach presented by Galfione et al. [17]. For each generated individual, the *gamultiobj* function computes the reconstructed deformed shape and compares it with the reference using the two error metrics presented in Eqs. (17) and (18) as objective functions

$$NRMSE = \frac{\sqrt{\frac{1}{n}\sum_{i=1}^{n}\sum_{j=1}^{3}\left(d_{i,j}^{Ref} - d_{i,j}^{SS}\right)^2}}{\|\boldsymbol{d}_{i_{max}}^{Ref}\|} \tag{17}$$

$$MDE = \frac{\|\boldsymbol{d}_{i_{max}}^{Ref} - \boldsymbol{d}_{i_{max}}^{SS}\|}{\|\boldsymbol{d}_{i_{max}}^{Ref}\|} \tag{18}$$

$$i_{max} = argmax(\|\boldsymbol{d}_{i}^{Ref}\|) \tag{19}$$

Here, $NRMSE$ stands for Normalized Root Mean Squared Error, and $MDE$ stands for Maximum Displacement Error. Then, $\boldsymbol{d}_i$ represents the displacement vector of the $i$-th node, while $d_{i,j}$ represents the $j$-th component of the displacement vector of the $i$-th node. Moreover, $d^{Ref}$ indicates a displacement component or vector of the reference deformed shape, while $d^{SS}$ indicates a displacement component or vector of the deformed shape reconstructed with shape sensing. Finally, $\boldsymbol{d}_{i_{max}}$ is the displacement vector at the node for which the magnitude of the displacement is maximum in the deformed shape, $n$ is the number of nodes, and $\|\cdot\|$ is an operator computing the Euclidean norm of the vector contained. These error metrics are valid for a case, such as the one

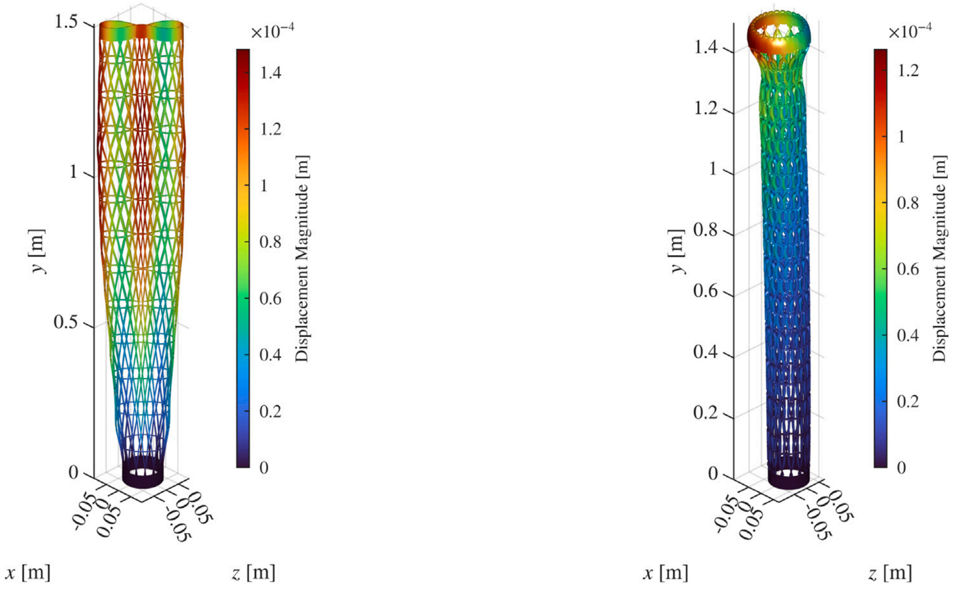

(a) MM reconstructed shape

(b) PCAM reconstructed shape

**Fig. 9.** Reconstructed deformed shapes with the two methods when all sensor locations are used. The reconstructed shapes with the minimum errors are shown. The shapes are plotted with a scale factor of 500.

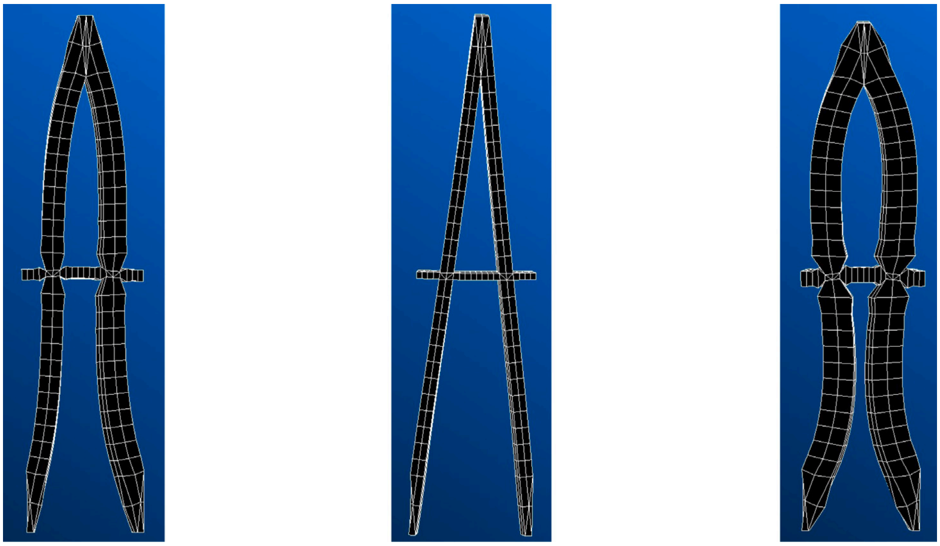

(a) Reference deformed shape (b) Normal Mode 1 (c) PCA-derived shape 1

**Fig. 10.** Zoom on a representative section of the deformed shapes, comparing the reference with the first normal mode and the first PCA-derived shape. White lines represent FE edges.

presented here, in which all displacement DOFs of each considered node are reconstructed; similar metrics can be designed when this is not the case. The number of strain sensors has been fixed at 16, as it is the number of channels in many acquisition systems. The acceptable locations for strain sensors are the nodes at which strain is exported for both the static and modal analyses presented above. These nodes, as described in Section 4.2.2, are those with two characteristics: they are only nodes of helic elements, and they are at the middle of the outside faces of the helicoidal struts. These nodes are shown in Fig. 8 for clarification.

Although the built-in *gamultiobj* MATLAB function is used here, some non-standard options are used to accommodate the nature of this optimization problem. The problem was defined as finding the best 16-sensor configuration, with respect to the two error metrics presented above. Each individual generated by *gamultiobj* is a vector of 16 integer numbers between 1 and the maximum number of possible locations (in this case, 7392). To obtain this type of individual, all 16 variables are defined as integers, with the lower bound set to 1 and the upper bound equal to the number of acceptable locations. Two additional considerations have been implemented to avoid sensor repetition within each individual, which could result in having more bases than sensors, thereby altering the problem's nature. First, a custom initial population is defined as a Latin hypercube sample generated by the MATLAB *lhsdesign* function [49]. This population (defined between 0 and 1) is rescaled between the lower and upper bounds, and then each value is rounded to the closest integer using the MATLAB *round* function [50]. Finally, any repeated number in a single individual is replaced with a different randomly generated number. This approach ensures that the initial population contains no individuals with repeated values. However, repetitions may still occur in individuals of subsequent generations, since *gamultiobj* has no option to prevent them. The approach adopted here is to avoid critical cases in which the number of unique sensors is less than or equal to the number of bases. This is obtained by defining a condition in the fitness (or objective) function for which, if the number of unique sensors is not larger than the number of bases, the shape sensing process is not performed, and both objectives are set to *Inf*.

The *gamultiobj* function returns a set of Pareto optimal individuals, with the corresponding objective function values. However, here the interest is in a single individual, who is then selected as the one with the smallest Euclidean norm of the vector of objective function values.

**Table 4**
Error metrics for varying basis selection thresholds for the MM and PCAM when OSP is performed.

| Method | Basis selection threshold | # Bases selected | NRMSE | MDE |
|---|---|---|---|---|
| MM | 0.0002% | 1 | (53.68 ± 0.60)% | (77.22 ± 0.41)% |
| MM | 0.0003% | 3 | (54.25 ± 1.50)% | (43.10 ± 1.94)% |
| MM | 0.0004% | 5 | (47.15 ± 1.50)% | (33.17 ± 2.15)% |
| MM | 0.0005% | 11 | (36.89 ± 4.21)% | (32.18 ± 2.55)% |
| PCAM | 70% | 2 | (35.19 ± 0.48)% | (31.37 ± 0.46)% |
| PCAM | 80% | 2 | (35.04 ± 0.47)% | (31.59 ± 0.67)% |
| PCAM | 90% | 3 | (17.19 ± 0.52)% | (20.07 ± 0.50)% |
| PCAM | 95% | 5 | (10.60 ± 0.19)% | (2.14 ± 0.79)% |
| PCAM | 99% | 6 | (10.54 ± 0.17)% | (2.20 ± 0.90)% |
| PCAM | 99.9% | 7 | (10.58 ± 0.22)% | (1.86 ±0.99)% |

## 5. Results and discussion

The two methods, MM and PCAM, are compared using the two error metrics presented in Eqs. (17) and (18). First, the comparison is conducted assuming that all strain-sensor locations are instrumented; thus, 7392 strain sensors are used. These results are presented by varying the basis selection thresholds, $e_{th}$ for the MM (Eq. (6)) and $\sigma_{th}$ for the PCAM (Eq. (8)), to investigate their impact on reconstruction accuracy, as shown in Table 3. Comparing these results, two important aspects are clear. First, the accuracy obtained with the best PCAM solution is much higher on both error metrics than that of the MM. Second, the first 100 natural modes of the structure can only reconstruct less than the 0.0006% of the static strain energy, meaning basically none of the modes are relevant for the reconstruction in this case. This is confirmed by comparing the best reconstructed shapes obtained with each method, presented in Fig. 9, with the reference deformed shape in Fig. 7(b). These figures qualitatively show that the PCAM-reconstructed shape is very close to the reference, whereas the MM-reconstructed shape is very different. As mentioned in Sections 4.3 and 4.4, to provide further information on these results, the deformed shapes of the first 11 normal modes by strain energy contribution are shown in Appendix B. In the same appendix, the deformed shapes of the first 7 PCA-derived shapes

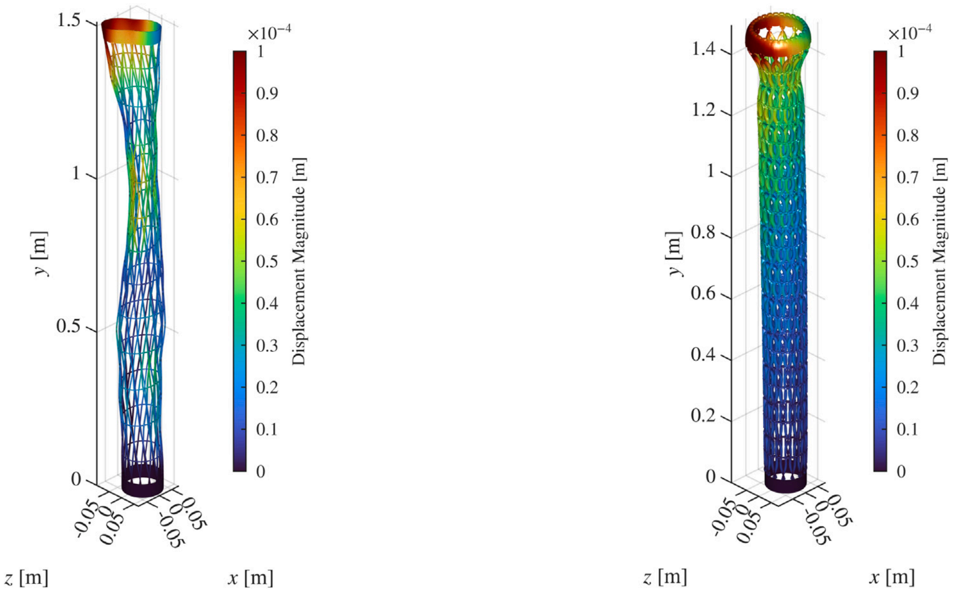

(a) MM reconstructed shape

(b) PCAM reconstructed shape

**Fig. 11.** Reconstructed deformed shapes with the two methods when OSP is performed. The reconstructed shapes with the minimum errors are shown. The shapes are plotted with a scale factor of 500.

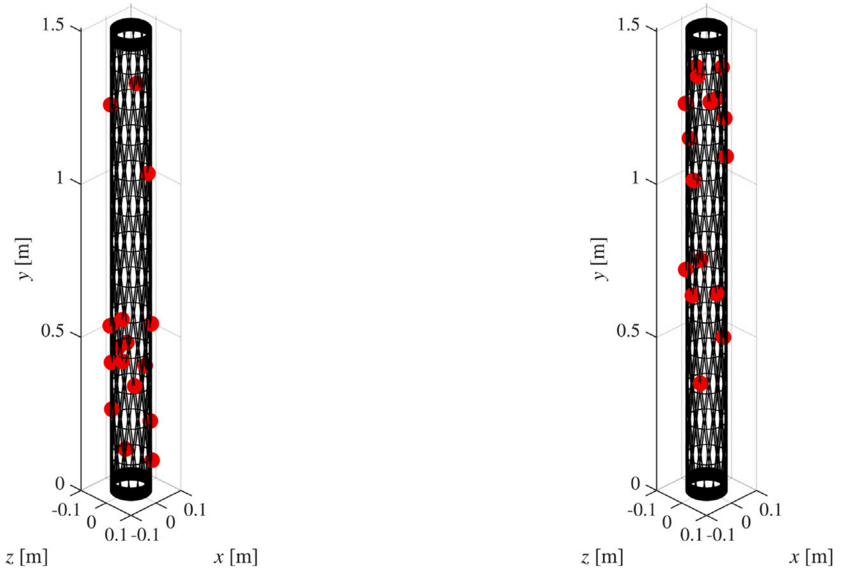

(a) Optimal sensor configuration for the MM

(b) Optimal sensor configuration for the PCAM

**Fig. 12.** Optimal sensor configurations resulting from the OSP for the MM and PCAM. These configurations are the ones that produce the reconstructions shown in Fig. 11. Each red dot represents a strain sensor.

are also shown. A relevant remark should be made about small but significant differences between the deformed shapes of the normal modes and the PCA-derived shapes. For instance, comparing Normal Mode 1 and Normal Mode 2, Fig. 13(f) and (h) respectively, with the first two PCA-derived shapes, Fig. 14(a) and (b), they look globally similar apart from a rescaling factor. The reason the normal modes do not produce results with the same accuracy as the PCA-derived shapes is local effects, as shown in Fig. 10. Looking at this zoomed-in section, it is clear that the variation in CTE at the intersection of helic elements results in bending phenomena and local strains in the reference that cannot be captured by the normal modes, but are present in the PCA-derived shapes.

Another interesting aspect of the comparison arises when performing the OSP. As mentioned above, the objective of this part of the investigation is to determine whether the proposed method is applicable under limited sensor availability. This is done by finding an optimal 16-sensor configuration for each value of the basis selection threshold. Here, the term optimal refers to a configuration that minimizes the error metrics on the considered load case. The results are presented in Table 4 using the same basis selection thresholds as for the non-optimized sensor

**Table 5**
Computational cost to obtain the bases for the two methods.

| Method | Wall time |
|---|---|
| MM | $116s$ |
| PCAM | $108s$ |

configurations. For each basis selection threshold, the OSP is repeated 30 times, and the error metrics are reported as the mean ± standard deviation computed with the built-in MATLAB *std* function [51]. A first remark regarding these results is the absence of the final basis selection threshold previously used in the MM (0.0006%). That threshold yielded 100 selected modes, resulting in more modes than sensors when the OSP was performed, an unfeasible condition. As before, the difference in error metrics between the two methods is substantial, with PCAM largely outperforming MM. The best accuracies obtained with the PCAM when OSP is performed are close to those obtained in the non-optimized case. However, a difference between the optimized and non-optimized PCAM results is evident: optimization yields more accurate local results and less accurate global results. In fact, the lowest $NRMSE$ is obtained for the non-optimized case, whereas the lowest $MDE$ is achieved by the optimized configurations. The accuracy of the PCAM can also be qualitatively verified in Fig. 11, where the best reconstructed shape with the MM and the PCAM are plotted. These deformed shapes were obtained using the sensor configurations shown in Fig. 12. Clearly, the MM cannot reconstruct the reference deformed shape (Fig. 7(b)), whereas the PCAM produces a very good result.

A final remark concerns the computational cost of obtaining the bases for the two methods. As mentioned in Section 3, the computational cost is distributed differently in the methods, and the final values depend on the number of normal modes to compute for the MM as well as the number of load cases considered for the PCAM. To provide a benchmark, the computational costs for the analyses performed here are presented in Table 5. The analyses were performed on a laptop with a 10-core *AMD Ryzen AI 9 365W/ Radeon 880M (2.00 GHz)* CPU and 32 GB (5600 MT/s) of memory. The cost presented for the MM is the cost of the modal analysis performed with MSC Nastran, whereas the cost for the PCAM is the sum of the costs of the two static structural analyses, also performed with MSC Nastran. The first static analysis aimed to obtain displacement fields from the polynomial temperature distributions, whereas the second aimed to obtain strain fields corresponding to the PCA-derived displacements. The difference between the two is small, although the PCAM cost could be slightly reduced by considering only the selected shapes rather than all shapes, as done here. Both computational costs presented here are for the preliminary steps required to obtain the ingredients for the shape sensing process. The cost of the actual shape sensing is identical for the two methods, as long as the same number of bases are selected, and consists of computing Eqs. (5) or (9). The cost of this computation is typically small enough to allow real-time monitoring with the MM, a property that is definitely retained in the PCAM. In real-time monitoring, the cost is especially low since, as mentioned above, the computation reduces to a matrix-vector multiplication.

## 6. Conclusions and future work

This work presents a new shape-sensing method derived as a variant of the Modal Method (MM), here referred to as the Principal Component Analysis-based Method (PCAM). In the PCAM, the structure's normal modes are replaced with alternative shapes computed through a four-step process. First, a set of relevant loads is defined. Second, loads are applied to the structure, and the resulting deformed shapes are computed via FE analysis. Third, PCA is performed on the obtained displacement fields, yielding a new ordered set of displacement fields that serve as the bases for the shape sensing process. Finally, the corresponding strain fields are obtained by applying the displacement fields to the structure in FE analyses. This new method can retain more information than the MM in the base shapes and therefore outperform it, especially when very local effects, unrelated to the structure's inertia, are involved.

The PCAM is then tested and compared with the MM in a relevant case study: the shape sensing of a boom segment for large deployable reflectors (LRBOOM) under non-uniform thermal loads. This structure presents several challenges and interesting aspects that render the MM inapplicable for shape sensing under these conditions. The main challenges are, on one hand, the nature of the loads (thermal) and, on the other hand, the material's anisotropy, which, combined with the complex geometry, produces locally sharp variations in the coefficient of thermal expansion in both magnitude and direction. These local effects are not captured by the structure's first normal modes, which arise from structural inertia, and therefore cannot be reconstructed by the MM, which yields highly inaccurate results. In contrast, in the PCAM, the bases are generated from temperature distributions and therefore inherently capture local thermal effects. Given its practical relevance, this study also investigates the applicability of the PCAM under limited sensor availability by performing an OSP that reduces the number of sensors to 16. The results show good accuracy for the PCAM, even with a limited number of sensors, a typical advantage of the MM compared to traditional alternatives that is retained in the new method.

To conclude, the PCAM showed promising results as an alternative to the MM in a case in which the latter performed poorly, but it was the only applicable method for structural complexity and sensor scarcity. In general, the literature lacks thorough validation of shape sensing algorithms for reconstructing thermal deformations. This work highlights that methods developed for shape sensing of structural deformations may not be suitable for different types of loads and proposes an alternative to a well-known shape-sensing algorithm, demonstrating its applicability to reconstructing thermal deformations of complex structures even under limited sensor availability. However, further numerical and experimental validation of this method is needed to demonstrate its usefulness and identify other relevant applications where current methods may falter.

## CRediT authorship contribution statement

**Alessio Galfione:** Writing – review & editing, Writing – original draft, Investigation, Formal analysis, Data curation, Conceptualization. **Marco Esposito:** Writing – review & editing, Supervision, Formal analysis, Conceptualization. **Giovanni Totaro:** Writing – review & editing, Resources, Project administration, Conceptualization. **Monica Ciminello:** Writing – review & editing, Conceptualization. **Salvatore Ameduri:** Writing – review & editing, Supervision, Resources, Conceptualization. **Marco Gherlone:** Writing – review & editing, Supervision, Resources, Funding acquisition, Formal analysis, Conceptualization.

## Declaration of competing interest

The authors declare the following financial interests/personal relationships which may be considered potential competing interests:

Alessio Galfione reports that financial support was provided by Italian Ministry of University and Research (MUR). If there are other authors, they declare that they have no known competing financial interests or personal relationships that could have appeared to influence the work reported in this paper.

## Acknowledgements

This publication is part of the project PNRR-NGEU which has received funding from the MUR - DM 117/2023. CIRA and POLITO authors would also like to acknowledge the Italian National Project LR-BOOM for the activities relevant to the boom test article.

## Appendix A. Strain energy from MSC nastran

In the commercial software MSC Nastran, used for structural analyses in this study, the quantity called *elemental strain energy* is computed as follows for linear elements subjected to temperature variations only [37]

$$E_e^* = \frac{1}{2}\boldsymbol{u}_e^T \boldsymbol{K}_e \boldsymbol{u}_e - \boldsymbol{u}_e^T \boldsymbol{P}_{et} \tag{20}$$

where $\boldsymbol{u}_e$ is the vector of element nodal dofs, $\boldsymbol{K}_e$ is the element stiffness matrix, and $\boldsymbol{P}_{et}$ is the element load vector equivalent to temperature variations. However, for the mode selection formulation, only the first term of $E_e^*$ in Eq. (20) is relevant [5]

$$E_e = \frac{1}{2}\boldsymbol{u}_e^T \boldsymbol{K}_e \boldsymbol{u}_e \tag{21}$$

Two options are here proposed for getting $E_e$ once $E_e^*$ is provided by MSC Nastran. The first one, and probably the easiest, is to obtain $\boldsymbol{u}_e$, $\boldsymbol{P}_{et}$, and $E_e^*$ as outputs from the analysis, and to simply compute $E_e$ as

$$E_e = E_e^* + \boldsymbol{u}_e^T \boldsymbol{P}_{et} \tag{22}$$

The second option is to enforce the computed $\boldsymbol{u}_e$ on the structure as BCs without any other mechanical or thermal load. Since in this second analysis $\boldsymbol{P}_{et} = \boldsymbol{0}$, the provided $E_e^*$ would correspond to the required $E_e$ (Eq. (20)). As noted above, this additional step is required when using MSC Nastran; however, other software may compute strain energy differently and may not require this correction.

## Appendix B. Bases for MM and PCAM

This appendix presents the deformed shapes of the bases used in the MM and the PCAM for shape sensing. Starting with the normal modes of the MM, the first 11 modes by strain-energy contribution are shown in Fig. 13 and the corresponding strain-energy contributions are shown in Table 6. These strain energy contributions are computed as described in Section 2 using all available strain sensors.

Then, the first 7 PCA-generated shapes used in the PCAM are plotted in Fig. 14, and the information on the corresponding variance is shown in Table 7.

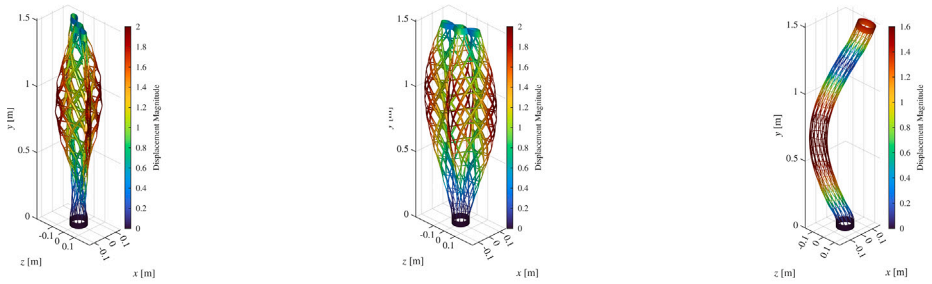

(a) Normal Mode 6 (b) Normal Mode 7 (c) Normal Mode 5

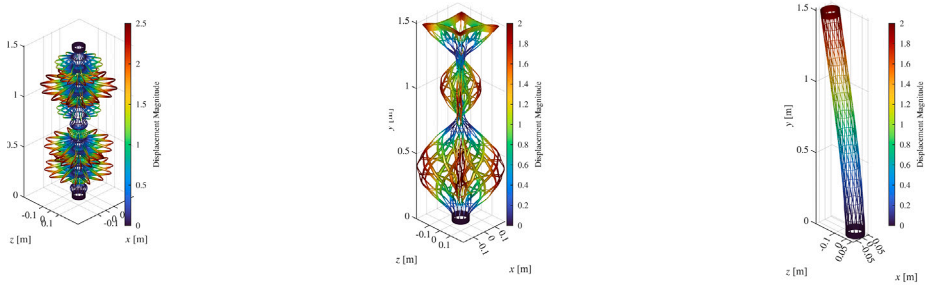

(d) Normal Mode 73 (e) Normal Mode 10 (f) Normal Mode 1

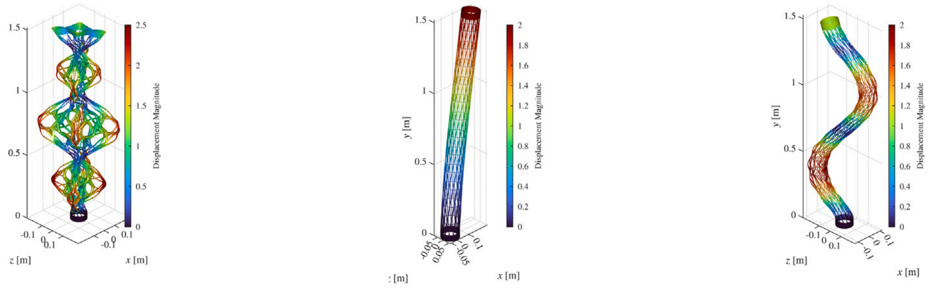

(g) Normal Mode 13 (h) Normal Mode 2 (i) Normal Mode 16

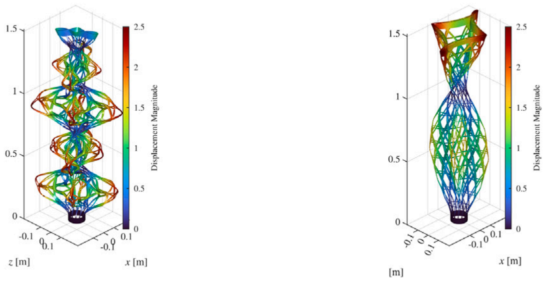

(j) Normal Mode 17 (k) Normal Mode 8

**Fig. 13.** Plots of the first 11 normal modes of the structure by strain energy contribution. They are all plotted with a scale factor of 0.1.

**Table 6**
Strain energy contributions of the first 11 normal modes.

| Mode Number | Strain energy contribution | Cumulative strain energy contribution |
|---|---|---|
| 6 | 0.0002167% | 0.0002167% |
| 7 | 0.0000731% | 0.0002899% |
| 5 | 0.0000524% | 0.0003423% |
| 73 | 0.0000511% | 0.0003935% |
| 10 | 0.0000300% | 0.0004234% |
| 1 | 0.0000237% | 0.0004471% |
| 13 | 0.0000151% | 0.0004623% |
| 2 | 0.0000148% | 0.0004772% |
| 16 | 0.0000110% | 0.0004882% |
| 17 | 0.0000084% | 0.0004966% |
| 8 | 0.0000078% | 0.0005044% |

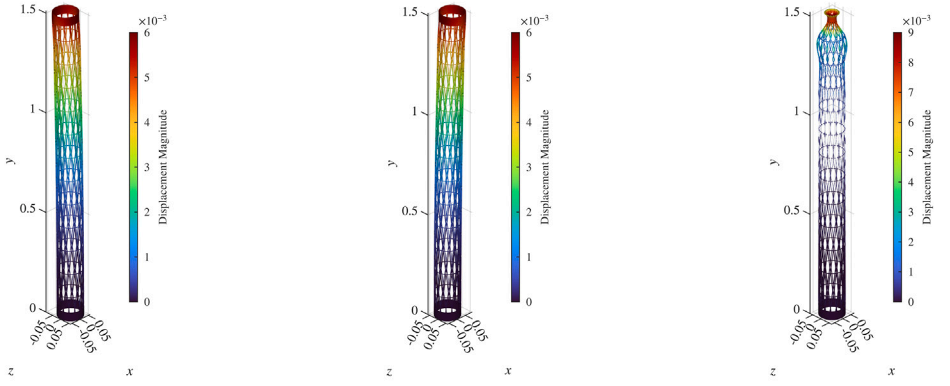

(a) PCA-derived shape 1 (b) PCA-derived shape 2 (c) PCA-derived shape 3

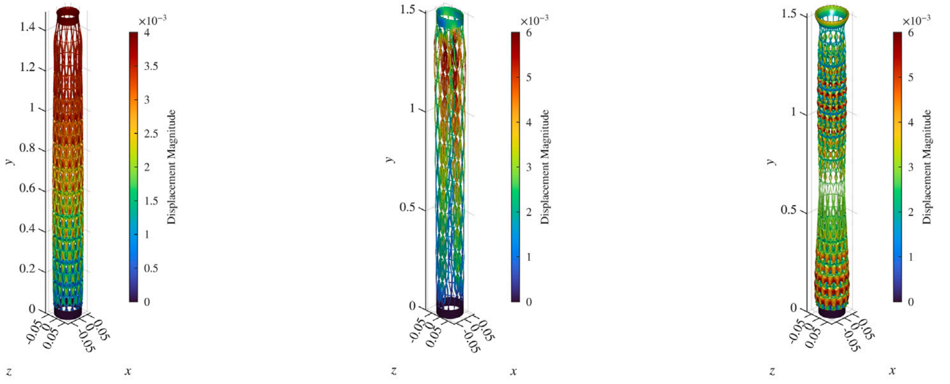

(d) PCA-derived shape 4 (e) PCA-derived shape 5 (f) PCA-derived shape 6

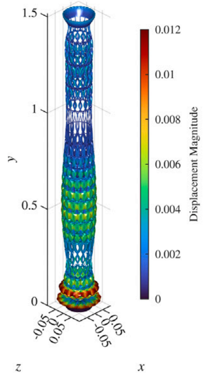

(g) PCA-derived shape 7

**Fig. 14.** Plots of the first 7 PCA-derived shapes. They are all plotted with a scale factor of 5.

**Table 7**
Variances of the first 7 PCA-generated shapes.

| Shape Number | Variance | Cumulative variance |
|---|---|---|
| 1 | 48.28% | 48.28% |
| 2 | 37.59% | 85.87% |
| 3 | 5.02% | 90.89% |
| 4 | 4.08% | 94.97% |
| 5 | 3.28% | 98.26% |
| 6 | 1.27% | 99.52% |
| 7 | 0.477086% | 99.999994% |

## Data availability

Data will be made available upon request.

## References

[1] Afonso F, Sohst M, Diogo CM, Rodrigues SS, Ferreira A, Ribeiro I, Marques R, Rego FF, Sohouli A, Portugal-Pereira J, Policarpo H, Soares B, Ferreira B, Fernandes EC, Lau F, Suleman A. Strategies towards a more sustainable aviation: a systematic review. Prog Aerosp Sci 2023;137:100878. https://doi.org/10.1016/j.paerosci.2022.100878. https://linkinghub.elsevier.com/retrieve/pii/S0376042122000707.

[2] Albers A, Rapp S, Heitger N, Wattenberg F, Bursac N. Reference products in PGE – product generation engineering: analyzing challenges based on the system hierarchy. Procedia CIRP 2018;70:469–74. https://doi.org/10.1016/j.procir.2018.02.046. https://linkinghub.elsevier.com/retrieve/pii/S2212827118304554.

[3] Atar C, Aktaş M. Advances in thermal modeling and analysis of satellites. Gazi Univ J Sci 2022;35:42–58. https://doi.org/10.35378/gujs.840191

[4] Bakalyar J, Jutte C. Validation tests of fiber optic strain-based operational shape and load measurements. In: 53rd AIAA/ASME/ASCE/AHS/ASC structures, structural dynamics and materials conference&lt;BR&gt;20th AIAA/ASME/AHS adaptive structures conference&lt;BR&gt;14th AIAA. Honolulu, Hawaii: American Institute of Aeronautics and Astronautics; 2012. https://doi.org/10.2514/6.2012-1904

[5] Bogert P, Haugse E, Gehrki R. Structural shape identification from experimental strains using a modal transformation technique. In: 44th AIAA/ASME/ASCE/AHS/ASC structures, structural dynamics, and materials conference. Norfolk, Virginia: American Institute of Aeronautics and Astronautics; 2003. https://doi.org/10.2514/6.2003-1626

[6] Brenneis M, Ibis M, Duschka A, Groche P. Towards mass production of smart products by forming technologies. Adv Mater Res 2014;907:113–25. https://www.scientific.net/AMR.907.113.

[7] Bruno R, Toomarian N, Salama M. Shape estimation from incomplete measurements: a neural-net approach. Smart Mater Struct 1994;3:92–7. https://doi.org/10.1088/0964-1726/3/2/002

[8] Bui-Thanh T, Willcox K, Ghattas O. Model reduction for large-scale systems with high-dimensional parametric input space. SIAM J Sci Comput 2008;30:3270–88. https://doi.org/10.1137/070694855

[9] Cerracchio P, Gherlone M, Tessler A. Real-time displacement monitoring of a composite stiffened panel subjected to mechanical and thermal loads. Meccanica 2015;50:2487–96. https://doi.org/10.1007/s11012-015-0146-8

[10] Chen J, Duan W, Yuan S, Zhang A. Deformation sensing of on-orbit large-scale antenna panel under non-uniform thermal load with regional integral ifem and improved element partition. 2024. https://doi.org/10.2139/ssrn.4695882. https://www.ssrn.com/abstract=4695882.

[11] Craiu ID, Nedelcu M. Combining iFEM and GBT for accurate shape sensing and damage detection in truncated conical shells with circular cross-section. Ocean Eng 2024;311:118811. https://doi.org/10.1016/j.oceaneng.2024.118811. https://linkinghub.elsevier.com/retrieve/pii/S0029801824021498.

[12] Esposito M, Gherlone M. Composite wing box deformed-shape reconstruction based on measured strains: optimization and comparison of existing approaches. Aerosp Sci Technol 2020;99:105758. https://doi.org/10.1016/j.ast.2020.105758. https://linkinghub.elsevier.com/retrieve/pii/S1270963819324538.

[13] Falle A, Wright E, Boley A, Byers M. One million (paper) satellites. Science 2023;382:150–2. https://doi.org/10.1126/science.adi4639

[14] Foss GC, Haugse ED. Using modal test results to develop strain to displacement transformations. In: Proceedings of the 13th international conference on modal analysis. Nashville; 1995.

[15] Freydin M, Rattner MK, Raveh DE, Kressel I, Davidi R, Tur M. Fiber-optics-based aeroelastic shape sensing. AIAA J 2019;57:5094–103. https://doi.org/10.2514/1.J057944

[16] Galasso B, Ameduri S, Concilio A, Totaro G, Spena P, Giusto G. Preliminary study of a shape reconstruction sensing architecture for space applications. In: 2023 14th international conference on mechanical and aerospace engineering (ICMAE). Porto, Portugal: IEEE; 2023. p. 513–7. https://doi.org/10.1109/ICMAE59650.2023.10424669.

[17] Galfione A, Meyer Zu Westerhausen S, Stauß T, Wawer ML, Ameduri S, Totaro G, Esposito M, Lachmayer R, Gherlone M. Methodology for consideration of different load cases in the design of a sensor-integrating, gentelligent antenna. In: Proceedings of the design society. Dallas, TX, USA; 2025. https://doi.org/10.1017/pds.2025.10254

[18] Gherlone M, Cerracchio P, Mattone M. Shape sensing methods: review and experimental comparison on a wing-shaped plate. Prog Aerosp Sci 2018;99:14–26. https://doi.org/10.1016/j.paerosci.2018.04.001. https://linkinghub.elsevier.com/retrieve/pii/S037604211730221X.

[19] Gherlone M, Cerracchio P, Mattone M, Di Sciuva M, Tessler A. Shape sensing of 3D frame structures using an inverse finite element method. Int J Solids Struct 2012;49:3100–12. https://doi.org/10.1016/j.ijsolstr.2012.06.009. https://linkinghub.elsevier.com/retrieve/pii/S0020768312002648.

[20] Gherlone M, Cerracchio P, Mattone M, Di Sciuva M, Tessler A. An inverse finite element method for beam shape sensing: theoretical framework and experimental validation. Smart Mater Struct 2014;23:045027. https://doi.org/10.1088/0964-1726/23/4/045027

[21] Giusto G, Totaro G, Spena P, De Nicola F, Di Caprio F, Zallo A, Grilli A, Mancini V, Kiryenko S, Das S, Mespoulet S. Composite grid structure technology for space applications. Mater Today Proc 2021;34:332–40. https://doi.org/10.1016/j.matpr.2020.05.754. https://linkinghub.elsevier.com/retrieve/pii/S2214785320343674.

[22] Go MS, Noh HK, Hyuk Lim J. Real-time full-field inference of displacement and stress from sparse local measurements using physics-informed neural networks. Mech Syst Signal Process 2025;224:112009. https://doi.org/10.1016/j.ymssp.2024.112009. https://linkinghub.elsevier.com/retrieve/pii/S0888327024009075.

[23] Gundlach J, Böswald M, Sodja J. Uncertainty quantification for the modal shape sensing of structures undergoing geometrically non-linear deformation. 2025. https://doi.org/10.2139/ssrn.5189529.

[24] Jolliffe IT. Principal component analysis. 2nd, Springer, New York: Springer Series in Statistics; 2002.

[25] Jutte CV, Ko WL, Stephens CA, Bakalyar JA, Richards WL, Parker AR. Deformed shape calculation of a full-scale wing using fiber optic strain data from a ground loads test. 2011.

[26] Kefal A. An efficient curved inverse-shell element for shape sensing and structural health monitoring of cylindrical marine structures. Ocean Eng 2019;188:106262. https://doi.org/10.1016/j.oceaneng.2019.106262. https://linkinghub.elsevier.com/retrieve/pii/S0029801819304391.

[27] Kerschen G, Golinval JC, Vakakis AF, Bergman LA. The method of proper orthogonal decomposition for dynamical characterization and order reduction of mechanical systems: an overview. Nonlinear Dyn 2005;41:147–69. https://doi.org/10.1007/s11071-005-2803-2

[28] Kirchner E, Wallmersperger T, Gwosch T, Menning JDM, Peters J, Breimann R, Kraus B, Welzbacher P, Küchenhof J, Krause D, Knoll E, Otto M, Muhammedi B, Seltmann S, Hasse A, Schäfer G, Lohrengel A, Thielen S, Stiemcke Y, Koch O, Ewert A, Rosenlöcher T, Schlecht B, Prokopchuk A, Henke EM, Herbst F, Matthiesen S, Riehl D, Keil F, Hofmann K, Pape F, Konopka D, Poll G, Steppeler T, Ottermann R, Dencker F, Wurz MC, Puchtler S, Baszenski T, Winnertz M, Jacobs G, Lehmann B, Stahl K. A review on sensor-integrating machine elements. Adv Sens Res 2024;3:2300113. https://doi.org/10.1002/adsr.202300113

[29] Ko WL, Richards WL, Fleischer VT. Applications of KO displacement theory to the deformed shape predictions of the doubly-tapered ikhana wing. 2009.

[30] Ko WL, Richards WL, Tran VT. Displacement theories for in-flight deformed shape predictions of aerospace structures. NASA/TP 2007-214612 NASA Technical Report Server; 2007. https://ntrs.nasa.gov/api/citations/20070032936/downloads/20070032936.pdf.

[31] Krysl P, Lall S, Marsden JE. Dimensional model reduction in non-linear finite element dynamics of solids and structures. Int J Numer Methods Eng 2001;51:479–504. https://doi.org/10.1002/nme.167

[32] Li Y, Ni P, Sun L, Xia Y. Finite element model-informed deep learning for equivalent force estimation and full-field response calculation. Mech Syst Signal Process 2024;206:110892. https://doi.org/10.1016/j.ymssp.2023.110892. https://linkinghub.elsevier.com/retrieve/pii/S0888327023008002.

[33] Lifson M, Arnas D, Avendaño M, Linares R. Low-earth-orbit packing: implications for orbit design and policy. J Spacecr Rockets 2025;62:452–65. https://doi.org/10.2514/1.A35913

[34] Liuzzo G, Parisi M, Fanelli P. Modal shapes selection criterion for modal reconstruction aimed at structural health monitoring. In: AIAS 2024. MDPI; 2025. p. 39. https://doi.org/10.3390/engproc2025085039. https://www.mdpi.com/2673-4591/85/1/39.

[35] Mao Z, Todd M. Comparison of shape reconstruction strategies in a complex flexible structure. In: Tomizuka M, editor. The 15th international symposium on: smart structures and materials & nondestructive evaluation and health monitoring. San Diego, California; 2008. https://doi.org/10.1117/12.775931. p. 69320H.

[36] Meyer Zu Westerhausen S, Kyriazis A, Hühne C, Lachmayer R. Design methodology for optimal sensor placement for cure monitoring and load detection of sensor-integrated, gentelligent composite parts. Proc Des Soc 2024;4:673–82. https://doi.org/10.1017/pds.2024.70. https://www.cambridge.org/core/product/identifier/S2732527X24000701/type/journal_article.

[37] MSC. Quick reference guide - MSC nastran 2024.2. Technical Report HEXAGON; 2024.

[38] Nedelcu M. Optimisation of inverse finite element method for shape sensing of thin-walled cylinders by using generalised beam theory. Thin-walled Struct 2023;188:110865. https://doi.org/10.1016/j.tws.2023.110865. https://linkinghub.elsevier.com/retrieve/pii/S0263823123003439.

[39] Nishio M, Mizutani T, Takeda N. Structural shape reconstruction with consideration of the reliability of distributed straindata from a brillouin-scattering-based optical fiber sensor. vol. 19. IOP Publishing; 2010, 035011.

[40] Pan X, Zhan Y, Zeng G, Wang X. TT&C capacity analysis of mega-constellations: how many satellites can we support? In: ICC 2022 - IEEE international

conference on communications. Seoul, Korea, Republic of: IEEE; 2022. p. 2393–8. https://doi.org/10.1109/ICC45855.2022.9838447. https://ieeexplore.ieee.org/document/9838447/.

[41] Pisoni AC, Santolini C, Hauf DE, Dubowsky S. Displacements in a vibrating body by strain gauge measurements. In: Proceedings of the 13th international conference on modal analysis; 1995.

[42] Qiu Y, Arunachala PK, Linder C. SenseNet: a physics-informed deep learning model for shape sensing. J Eng Mech 2023;149:04023002. https://doi.org/10.1061/JENMDT.EMENG-6901

[43] Raissi M, Perdikaris P, Karniadakis G. Physics-informed neural networks: a deep learning framework for solving forward and inverse problems involving non-linear partial differential equations. J Comput Phys 2019;378:686–707. https://doi.org/10.1016/j.jcp.2018.10.045. https://linkinghub.elsevier.com/retrieve/pii/S0021999118307125.

[44] Shkarayev S, Krashantisa R, Tessler A. An inverse interpolation method utilizing in-flight strain measurements for determining loads and structural response of aerospace vehicles. In: Proceedings of the 3rd international workshop on structural health monitoring. Stanford University; 2001.

[45] Tessler A, Spangler JL. A variational principal for reconstruction of elastic deformation of shear deformable plates and shells. NASA/TM 2003–212445 NASA Technical Report Server; 2003. https://ntrs.nasa.gov/api/citations/20030068121/downloads/20030068121.pdf.

[46] Tessler A, Spangler JL. Inverse FEM for full-field reconstruction of elastic deformations in shear deformable plates and shells. In: 2nd European workshop on structural health monitoring; 2004.

[47] Tessler A, Spangler JL. A least-squares variational method for full-field reconstruction of elastic deformations in shear-deformable plates and shells. Comput Methods Appl Mech Eng 2005;194:327–39. https://doi.org/10.1016/j.cma.2004.03.015. https://linkinghub.elsevier.com/retrieve/pii/S0045782504003342.

[48] The MathWorks Inc. gamultiobj - multiobjective genetic algorithm; 2025. https://www.mathworks.com/help/gads/gamultiobj.html.

[49] The MathWorks Inc. lhsdesign - latin hypercube sample; 2025. https://www.mathworks.com/help/stats/lhsdesign.html.

[50] The MathWorks Inc. round - round to nearest decimal or integer; 2025. https://www.mathworks.com/help/matlab/ref/double.round.html.

[51] The MathWorks Inc. std - standard deviation; 2025. https://www.mathworks.com/help/matlab/ref/double.std.html.

[52] The MathWorks Inc. SVD - singular value decomposition; 2025. https://www.mathworks.com/help/matlab/ref/double.svd.html.

[53] Yu Z, Ma X, Zhu J, Zhang D, Xue Y, Huang P, Li Y, Li H. A deformation reconstruction strategy for integrated truss structures subjected to thermal–mechanical load. Sensors 2025;25:558. https://doi.org/10.3390/s25020558. https://www.mdpi.com/1424-8220/25/2/558.

[54] Zhang D, Wang T, Xu H, Wang B, Bi R, Zhao T, Qian P. An improved inverse finite element framework for shape sensing: application of SVD-based extended data-driven approach in preregression. IEEE Trans Instrum Meas 2025;74:1–9. https://doi.org/10.1109/TIM.2024.3522381. https://ieeexplore.ieee.org/document/10817613/.